J Mater Sci: Mater Electron
DOI 10.1007/s10854-017-7138-5

Does the pelletization pressure modify the effective anisotropy of the grains in (Bi,Pb)2223 bulk system?

A. Cruz-García[1] · E. Altshuler[2] · J. R. Fernández-Gamboa[1] · R. F. Jardim[3] · O. Vazquez-Robaina[4] · P. Muné[1]

Received: 20 March 2017 / Accepted: 12 May 2017

Abstract In this paper we present a new method to determine separately inter and intragranular magnitudes of polycrystalline superconducting materials, such as: intrinsic effective anisotropy, $t = \rho_c/\rho_{ab}$, the slope of the linear part in the temperature dependence of the ab-planes resistivity, $A_{ab} = \Delta\rho_{ab}/\Delta T$, the weak links resistivity, ρ_{wl}, and the orientation probability of the grains' a-axes along a certain preferential direction, γ_{xa}. Here, ρ_{ab}, ρ_c and T are the main values of the resistivity tensor and the measurement temperature, respectively. The application of the method, illustrated by two (Bi,Pb)2223 polycrystalline samples, allows comparing the parameters obtained for the grains with those reported in single crystals. Moreover, we have demonstrated that different compacting pressures in the fabrication of the pellets change not only the inter, but also the intragranular properties of the ceramics. The method could be used to follow the different steps during the synthesis of polycrystalline high T_c superconductors in order to optimise the process.

✉ P. Muné
mune@uo.edu.cu

A. Cruz-García
acruz@uo.edu.cu

[1] Departamento de Física, Universidad de Oriente, P. Lumumba s/n, 90500 Santiago de Cuba, Cuba

[2] Superconductivity Laboratory and Group of Complex Systems and Statistical Physics, IMRE-Physics Faculty, University of Havana, 10400 Havana, Cuba

[3] Departamento de Física dos Materiais e Mecânica, Instituto de Física, Universidade de São Paulo, CP 66318, São Paulo, SP 05315-970, Brazil

[4] LIEES Department, IMRE-Physics Faculty, University of Havana, 10400 Havana, Cuba

1 Introduction

The optimization of the synthesis process and the search of new superconducting compounds continue to be active areas of the superconductivity with fundamental and applied goals [1–8]. A prominent feature of several superconductors for large scale applications is their polycrystalline structure [5, 9]. Within this context, two essential issues should be taken into consideration when the performance of high critical temperature superconductors (HTS) is evaluated. One is the intergrain weak links [8] related with the low texture [5], porosity and the presence of spurious phases [5, 10, 11]. The other is the intragranular flux pinning [7], which is rather low in several HTS, because of their layered structure and high anisotropy.

Due to the reasons mentioned above several models to characterize separately intra and inter granular regions have been developed [12–14]. The idea is based on modelling the granular structure and obtaining the inter and intragranular properties starting from measurements performed in the granular sample as a whole.

A good example of the philosophy described before is reported in reference [15]. The authors used the magnetic hysteresis of the critical current density in granular superconductor, mainly ceramics, to determine the critical current density of the grains and their effective lower critical field by means of the Bean's model [16, 17]. However, parameters like the intrinsic effective anisotropy of the grains, $t = \rho_c/\rho_{ab}$, and the slope of the linear part in the temperature dependence of the ab-planes resistivity, $A_{ab} = \Delta\rho_{ab}/\Delta T$ were not studied in that work [15]. Here, ρ_c, ρ_{ab} and T are the out-of-plane resistivity, the in-plane resistivity and the temperature of the crystallites, respectively.

Published online: 01 June 2017

One possibility to estimate t and A_{ab}, starting from transport measurements in polycrystalline samples, is the combined modelling of the granular material by using the effective medium approximation (EMA) [18] besides the use of a phenomenological model reported elsewhere [19]. Such a combination resulted in a quantitative description of the anisotropy parameter at the level of the sample, μ, as a function of the orientation probability of the grains γ_{xa} and other magnitudes, already reported by Cruz-García and Muné [20]. However, in that paper, the model was applied to experimental data, extracted from the literature [19, 21, 22], which prevented the authors from estimating t and A_{ab} starting from the experimental data, mainly in the case of Bi-based samples. On the other hand, the volume fraction of pores in the polycrystalline samples was disregarded [20].

In this paper we have estimated the effective values of intrinsic intragranular anisotropy, $t = \rho_c/\rho_{ab}$, the slope of the linear part in the temperature dependence of the ab-planes resistivity, $A_{ab} = \Delta\rho_{ab}/\Delta T$, the weak links resistivity, ρ_{wl}, and the orientation probability of the grains' a-axes along a certain preferential direction, γ_{xa}, for two polycrystalline $Bi_{1.65}Pb_{0.35}Sr_2Ca_2Cu_3O_{10+\delta}$ ((Bi,Pb)2223) superconducting samples. The pellets were prepared by a solid-state reaction method and pressed uniaxially at two different compacting pressures before the last heat treatment.

Here, we are able to obtain the components of the resistivity tensor from overall transport measurements by combining models proposed by other authors: we will call the resulting technique "Levin-Gonzalez Method" (LGM) [23, 24]. The experimental data was then processed by using a theoretical model based on the EMA and the phenomenological model proposed by Díaz et al. [19], which correlates several parameters by means of two equations: $\mu = F(\mu, \gamma_{xa}, L_a/L_c, p, t)$ and $f_x = f_x(\mu, \gamma_{xa}, L_a/L_c, p, t)$. Here, μ, L_a/L_c, p and f_x represent the effective anisotropy parameter at the level of the sample, the shape anisotropy of the grains, the volume fraction of pores and the orientation factor of the grains for electrical transport measurements, respectively. All these parameters can be determined experimentally.

Thus, by solving the two equations system γ_{xa} and t can be found. Finally, A_{ab} can be also found as a function of some of the parameters determined experimentally and those obtained by solving the system equations.

Summarizing, we are offering a new method to separate inter and intragranular magnitudes of polycrystalline materials, starting from electrical transport measurements performed on polycrystalline pellet samples. The application of the method, illustrated by two (Bi,Pb)2223 polycrystalline samples, allows comparing the obtained results for the grains with those reported for single crystals in reference [25] and by Fujii in private communication. Moreover, we have demonstrated that different compacting pressures in the fabrication of the pellets change not only the inter, but also the intragranular properties of the ceramics. Complementary characterizations related to the microstructure of the samples, structural parameters of the crystallites and electrical transport measurements support the results of the method application.

2 Experimental details

Polycrystalline pellets of $Bi_{1.65}Pb_{0.35}Sr_2Ca_2Cu_3O_{10+\delta}$ were prepared from powders of Bi_2O_3, PbO, $SrCO_3$, $CaCO_3$, and CuO which were mixed in the atomic ratios of Pb:Bi:Sr:Ca:Cu (1.65:0.35:2:2:3). The mixture was first calcined in air at 750 °C for 40 h. After that, the powder was reground and pressed into pellets of 8 mm in diameter and 2 mm in thickness at a pressure of 196 MPa. These pellets were heat treated at 800 °C in air for 40 h. Subsequently, they were reground, pressed again, and sintered in air for 40 h at a temperature of 845 °C. This step was repeated three times, as described elsewhere [26]. Finally, the pellets were reground and pressed at two different uniaxial compacting pressures to obtain cylindrical samples with typical dimensions of 8 mm in diameter and 5 mm in height. The compacting pressures were 230 and 780 MPa for the GD0P1 and GD0P2 samples, respectively. The last heat treatment of the pellets was performed in air for 40 h at a temperature of 845 °C, followed by slow cooling.

The densities of the two samples compacted at different pressures were determined by means of the ratio of their masses and volumes. The volumes were determined considering the pellets as cylinders and determining their dimensions with a resolution of 0.05 mm. The masses were measured with a digital balance with resolution of 0.1 mg. With this measured density and the structural one, which in the case of Bi2223 is 6.3 g/cm^3 [27, 28], the volume fraction of pores of the samples, p was estimated.

The microstructure of the samples was studied by means of scanning electron microscopy (SEM) of fractured surfaces. The study was performed with a microscope model Hitachi S-530, which has nominal resolution range of ~ 30–40 nm operating within an interval of 15–20 kV. The platelet shape of the grains is revealed in both samples.

By using a Bruker-AXS D8 Advance X-ray diffractometer, we have identified the crystallographic phases in the powders before the last heat treatment. These measurements were performed at room temperature using Cu Kα radiation in the $3 \leq 2\theta \leq 60$ range with a 0.05° (2θ) step size and 6 s. counting time. From the X-ray diffraction patterns taken in pellet samples the texture of two specimens was evaluated by means of the Lotgering factors. In addition, a qualitative evaluation of the residual strains in the

Table 1 Dimensions of the samples.

Sample	Length (cm)	Width (cm)	Thickness (cm)
GD0P1	0.669	0.227	0.086
GD0P2	0.578	0.246	0.064

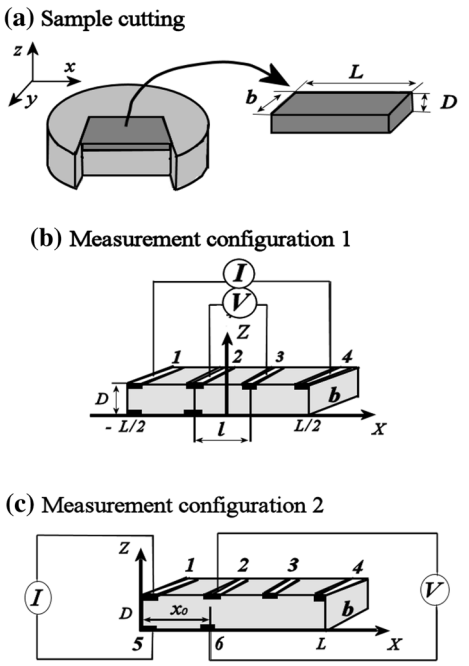

Fig. 1 Types of slabs extracted from a pellet and measurement configurations. **a** Slab to be measured using the LGM. **b** Experimental configuration used for the determination of the x-axis effective resistivity, ρ_x. **c** Experimental configuration used in the determination of the z-axis effective resistivity, ρ_z

pellets samples was performed comparing the positions of the peaks of the pellet samples with those that correspond to a powder sample.

In order to measure the temperature dependence of the electrical resistivity tensor and its components in the paracoherent state, the samples were cut from the pellets in slab form (see Fig. 1a) with typical dimensions displayed in Table 1. Electrical contacts were prepared using silver paint with a heat treatment at 730 °C for 20 min, these were as small as possible in order to minimize their effects on the voltage measurements. The typical relative contact size was about 10% of the block dimensions. Before each measurement, the samples were cooled from room temperature down to 80 K. The excitation current was injected according to the LGM [23, 24] as shown in Fig. 1b, c. Both the voltage across the sample and its temperature were collected while the temperature was raised slowly to 300 K for the case of the temperature dependence of the electrical resistivity tensor.

Regarding the measurements of the resistivity tensor components in the paracoherent state, in which the dissipation is mainly intergranular [19], the samples were cooled down to 103 K and the $I-V$ curve was taken. It was transformed into a resistivity versus current density curve starting from which the paracoherent resistivity tensor component was determined by taking the resistivity value at the point where the slope of the $\rho-J$ curve starts to decrease. Here, we are associating the change of the slope of the curve to the appearance of a new mechanism of dissipation linked to the intragranular planar defects [20, 29]. With this selection of the level of paracoherent resistivity we are avoiding the "contamination" of the measurements due to the presence of intragranular dissipation sources. It is clearly illustrated in subsection 3.2.

In both types of measurements described before six electrical contacts were placed on the upper and lower faces of the samples according to the sketch shown in Fig. 1b, c. In configuration 1, the current is injected through the contacts 1 and 4, while the potential differences on this face, V_x, are recorded between the contacts 2 and 3 (see Fig. 1b). In another measurement configuration the current is injected through the contacts 1 and 5, while the potential differences on this face, V_z, are recorded between the contacts 2 and 6 (see Fig. 1c). The two components of the electrical resistivity tensor ρ_x and ρ_z were calculated from these measurements and the dimensions of the sample through the Eqs. (24) and (25) presented in Appendix 6. Here, the dimensions of the samples shown in Table 1 were determined with a resolution of 0.01 mm.

3 Results and discussion

The diagram displayed in Fig. 2 sketches the procedure we will follow to get information from our samples. In subsections 3.1 and 3.2, we describe the measurements resulting in the different input parameters indicated at the top of the diagram. In subsection 3.3, we describe how the model works to obtain the parameters shown at the bottom of Fig. 2, and then we compare them back with the experiment in subsection 3.4.

3.1 Microstructural analysis and X-ray diffraction patterns

Table 2 displays a summary of the microstructural properties of the two samples studied in this paper. The densities of the samples substantially increase with increasing pressures and as a result a significant reduction of the volume fraction of pores is observed. Here, $p=(d_s-d_r)/d_s$, where d_r and d_s are the experimental and structural densities [28], respectively.

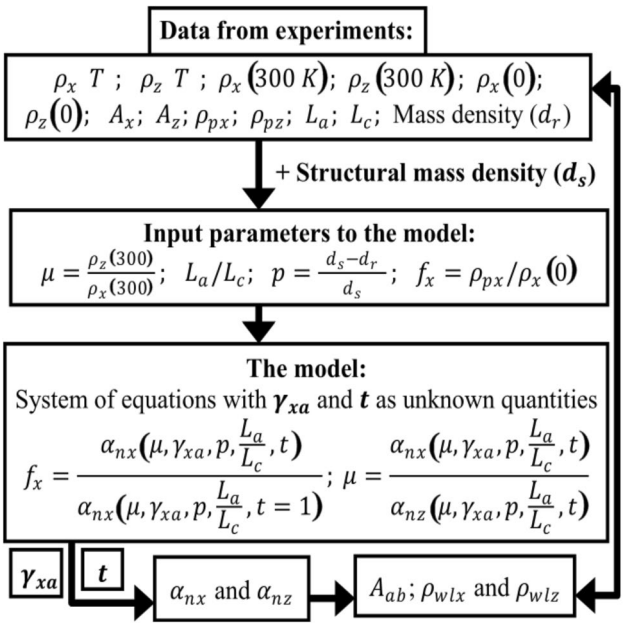

Fig. 2 Diagram of the method to separate the intra and intergranular parameters starting from microstructural and electrical transport characterizations

Table 2 Mass density, volume fraction of pores, p, and shape anisotropy of the grains, L_a/L_c.

Sample	Density (g/cm^3)	Volume fraction (p)	L_a/L_c
GD0P1	4.62	0.267	8.5
GD0P2	5.33	0.154	18.8

The effect of the compacting pressure has its counterpart in the microstructure of these samples. This can be inferred from the fracture micrographs of samples GD0P1 and GD0P2 which are shown in Fig. 3a, b, respectively. In both micrographs it is possible to observe that the granular morphology of both samples is similar, exhibiting grains with nearly platelet-like shape. A careful inspection also indicates changes in both the grain size and the grain orientation. The average grain size in the sample GD0P1 was found to be $L_a = (7.4 \pm 0.5)$ μm long and as thick as $L_c = (0.87 \pm 0.05)$ μm. For the sample GD0P2, the grains were found to have dimensions $L_a = (9.2 \pm 0.5)$ μm long and $L_c = (0.49 \pm 0.03)$ μm thick. The ratio L_a/L_c, which is referred to the mean aspect ratio of the grains [19], has been found to be very sensitive to the applied pressure and were 8.5 and 18.8 for the samples GD0P1 and GD0P2, respectively (see Table 2). These values are higher than those of 2.5 and 4.5 in ceramic samples of $YBa_2Cu_3O_{7-\delta}$ [19], but similar to those estimated for both (Bi,Pb)2223 superconducting bulk and tapes [21, 22, 30].

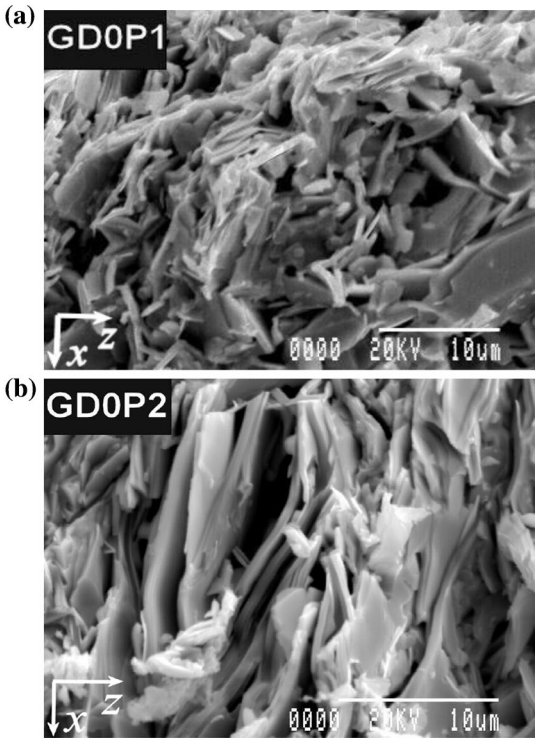

Fig. 3 Fracture micrographies of the samples obtained by SEM. **a** Sample GD0P1. **b** Sample GD0P2

Fig. 4a displays the X-ray diffraction pattern taken on a powder sample extracted from the GD0P1 sample.

The relative volume fractions of the high-T_c (Bi,Pb)2223 phase is calculated based on the following equation [1, 31, 32]:

$$f_H = \frac{\Sigma I_{H(hkl)}}{\Sigma I_{H(hkl)} + \Sigma I_{L(hkl)} + \Sigma I_{E_1(hkl)} + \Sigma I_{E_2(hkl)}} \quad (1)$$

Here, $I_{H(hkl)}$, $I_{L(hkl)}$, $I_{E_1(hkl)}$ and $I_{E_2(hkl)}$ are the intensities of the (hkl) diffraction lines for high-T_c , low-Tc ((Bi,Pb)2212), Ca_2PbO_4 and (Bi,Pb)2201 phases, respectively. When performing the calculation, the weight fractions of the (Bi,Pb)2223 phase are estimated to be 96% for both samples. For the (Bi,Pb)2223 phase, the unit-cell parameters were calculated assuming an orthorhombic unit cell and the obtained values $a = 5.3996$ Å, $b = 5.4117$ Å, and $c = 37.1140$ Å are in excellent agreement with those reported for the same compound elsewhere [1, 33].

Also, we have used the X-ray diffraction patterns shown in Fig. 4 to evaluate the following important features of both samples: (a) the residual strains due to the pelletization process (b) sample texture by means of the Lotgering factor calculated for the (00l) peaks.

The residual strains have been qualitatively evaluated by observing the displacement of the (00l) peaks. Such peaks

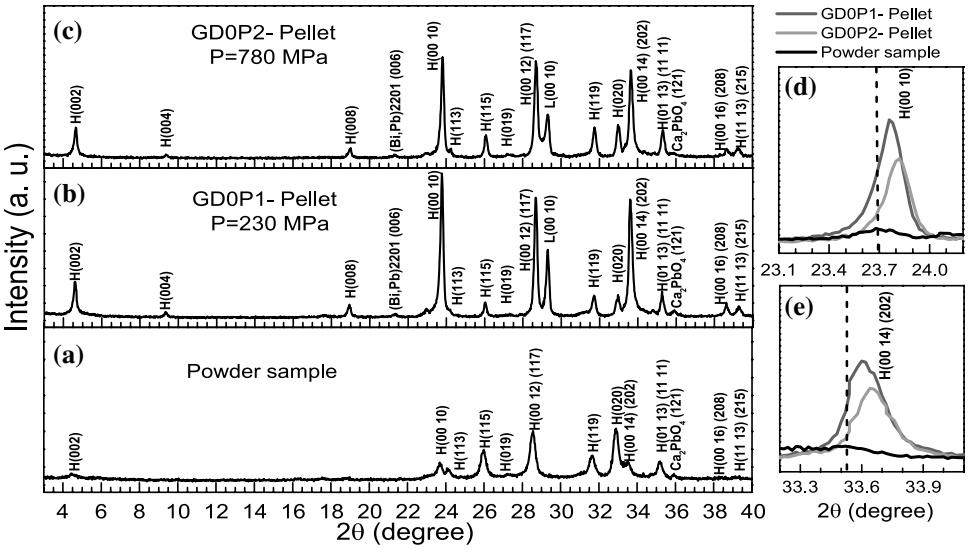

Fig. 4 X-ray diffraction patterns of powder and pellet samples. The reflections belonging to the (Bi,Pb)2223, (Bi,Pb)2212, Ca_2PbO_4 and (Bi,Pb)2201 phases are marked by "H", "L", "Ca_2PbO_4" and "(Bi,Pb)2201", respectively. Panels (**d**) and (**e**) show the displacement of two peaks due to the residual strains. The main peaks display their Miller's indexes.

that belong to the GD0P2 are dislocated to a greater 2θ values as compared with those that correspond to GD0P1. It means that uniform stresses are present and these increase with increasing pelletization pressures [34]. This may induce structural defects in the crystallites modifying their electrical transport properties. The discontinue lines in Fig. 4d, e represent the position of the peak for the powder sample which is assumed free of strains.

The Lotgering factors were calculated by means of the formula [35, 36]:

$$F = (P - P_0)/(1 - P_0), \tag{2}$$

where,

$$P = \sum_{l} I(00l) / \sum_{hkl} I(hkl). \tag{3}$$

Here, I refers to the X-ray peak intensity; P is the sum of the integrated intensities for all $(00l)$ reflections divided by the sum of all intensities of (hkl) in the textured specimen. P_0 is an equivalent parameter for a random specimen taken from the powder sample. An apparently contradictory result was obtained. The Lotgering factor of the samples decreases with increasing pressures from 0.34 to 0.24 for GD0P1 and GD0P2 samples, respectively. A possible explanation is an increase of the defect density due to mechanical deformation of the crystallites at high pressures. It is very important to highlight that even when the grains display to be more oriented among them in GD0P2 sample, the crystallites inside each grain could be more disoriented due to the creation of intragranular defects induced by the pelletization process.

Finally, an important feature of the x-ray diffraction patterns to be mentioned here, it is the presence of the (00 10) peak that correspond to the low T_c phase in both pellet samples, but it is absent in the powder one. Everything indicates that a thin layer of the (Bi,Pb)2212 phase is covering the compaction surface of the sample on which the X-rays were reflected.

As we will see in the subsections 3.2 and 3.4 these main microstructural features of the pellet samples have their counterparts in the electrical transport measurements.

3.2 Electrical transport measurements

Now the experimental data displayed in the first block of the diagram shown in Fig. 2 is completed. The values are shown in Table 3. The parameters $\rho_x(0)$, $\rho_z(0)$, A_x and A_z, are obtained by linear fitting of the curves of electrical

Table 3 Slopes of the electrical resistivity at the sample level, A_x and A_z, residual electrical resistivities, $\rho_x(0)$ and $\rho_z(0)$, electrical resistivities at 300 K, ρ_x and ρ_z

Sample	Slope A_x (μΩ cm/K)	Slope A_z (μΩ cm/K)	$\rho_x(0)$ (mΩ cm/K)	$\rho_z(0)$ (mΩ cm/K)	$\rho_x(300)$ (mΩ cm/K)	$\rho_z(300)$ (mΩ cm/K)	μ (300 K)	ρ_{px} (mΩ cm/K)	f_x
GD0P1	5.720	108.400	0.681	12.420	2.393	44.862	18.750	0.188	0.276
GD0P2	3.540	143.200	0.385	14.600	1.442	57.353	39.760	0.147	0.382

All previous values were obtained in the two principal directions of the sample. Besides are shown the external electrical anisotropy, μ, the para-coherent resistivity in x-direction, ρ_{px}, and the orientation factor of the grains, f_x

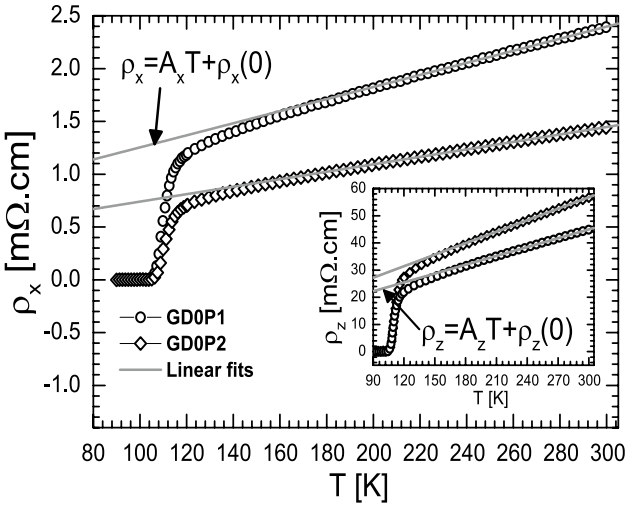

Fig. 5 Temperature dependencies of the resistivity tensor component, $\rho_x(T)$, of the samples GD0P1 and GD0P2. The inset shows the temperature dependencies of resistivity tensor component, $\rho_z(T)$, of the same samples. Some physical parameters extracted from $\rho_i(T)$ $i = x, z$ curves are displayed in Table 2 and discussed in the text.

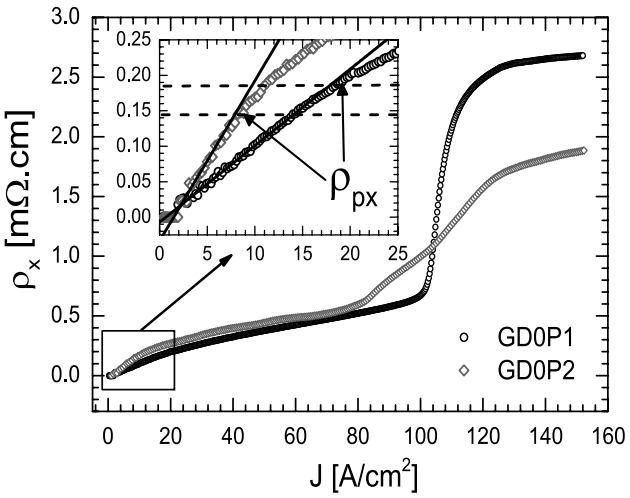

Fig. 6 The mean current density dependencies of x-axis resistivity, $\rho_x(J)$ for the samples GD0P1 and GD0P2, measured at constant temperature $T =$ K. The inset shows the measurement method to obtain the paracoherent resistivity, ρ_{px}.

resistivity dependence with the temperature in the linear region at high temperatures (see the fitting line and the equations inserted in Fig. 5). Here A_x, A_z are the slopes of the electrical resistivity and the $\rho_x(0)$, $\rho_z(0)$ the residual electrical resistivity in the two principal directions of the sample, respectively.

In Fig. 6 the way of determining the paracoherent resistivity, ρ_{px} of each sample is displayed. The ρ_{px} value is selected in the point where the straight line separates from $\rho_x - J$ curve (see the inset in Fig. 6). The explanation of this method of selection has been also discussed elsewhere [20]. It is related to the fact that the $\rho_x - J$ curves of the samples GD0P1 and GD0P2 have slopes different from zero in the region of current densities 20–100 A/cm^2. This behavior is a consequence of the intragranular dissipation that may affect the determination of the orientation factor of the grains.

Moreover, for low values of current density in the Fig. 6, the difference between both curves is small, and the sample GD0P1 exhibits a characteristic behavior of ceramic samples [19]. The transition to the normal state of the crystallites occurs close to the current density of 100 A/cm^2 in one step. However, a double step transition is observed for sample GD0P2, since it shows a significant change of the slope in its curve of $\rho_x - J$ around 80 A/cm^2. As a result, both curves are clearly separated reaching the normal state resistivity for $J > 130$ A/cm^2. We will be back on this issue later. Finally, by using some of the magnitudes experimentally determined the input parameters of the model are calculated as displayed in the second block in Fig. 2.

3.3 Modeling an anisotropic granular superconductor

A model similar to this that we present here was previously published by us [20]. It is based on two main ideas. First, the resistivity of the polycrystalline sample can be written as

$$\rho = \frac{1}{\alpha_n}(\rho_{ab} + \rho_{wl}). \tag{4}$$

Equation (4) expresses that the resistivity of the sample depends on the in-plane resistivity of the crystallites plus the resistivity of the Josephson junctions or weak links. This sum is amplified by a factor $1/\alpha_n$ that represents the combined effects of the grains' misalignment and the defects in the polycystalline sample. Here, $\rho_{ab} = A_{ab}T$ and $\alpha_n = f\alpha_{str}$ where α_{str} represents the effects of the defects on the resistivity of the sample [19]. When we compare (4) with the linear part of experimental dependence $\rho(T)$,

$$\rho = AT + \rho(0), \tag{5}$$

$A_{ab}/\alpha_n = A$ and $\rho_{wl}/\alpha_n = \rho(0)$ are obtained easily [13, 14, 19].

In the case of a sample with two main directions, Eqs. (4) and (5) should be written for each of them [20]. If μ does not depend on the temperature or has a weak dependence with it, then one may take $\mu = \alpha_{nx}/\alpha_{nz}$ where x and z are the two main directions of the samples. Here, z is taken along the compacting direction and x is perpendicular to it. For high T_c superconductors, like YBCO and Bi-based

samples, have a very high intragranular anisotropy parameter in the range $10^2 - 10^4$ [25, 37, 38]

The orientation factor of the grains, f_x, have been expressed as a function of the orientation probability along the x-axis, γ_{xa}, the shape anisotropy of the grains, L_a/L_c, and the intrinsic effective anisotropy of the grains, t, as already was reported elsewhere [20]. The calculations are based on EMA [18], which constitutes the second pillar of the model: here it is assumed the pollicrystalline sample made up of two different phases represented by the grains oriented with their a or b axes parallel to the x-axis of the sample and those with their c axes oriented along the x-axis of the sample, respectively. Thus, the orientation probability, γ_{xa}, can be also interpreted as the probability of finding the first phase in the polycrystalline sample.

In this paper we will use a similar description to that presented before [20], but modified in some aspects. Here, we are including a new phase in the calculations of the effective conductivity, which accounts for the pores. These will be assumed spherical with conductivity zero, probability of appearance, p, and randomly distributed inside the polycrystalline sample. Moreover, all the contributions of the defects to the resistivity of the polycrystalline sample will be included in this new phase. Finally, in the present approach, the effects of the grains' disorientation and defects are not separated in two factors, but contained in the same fraction α_n.

In Appendix 5 the calculations to obtain the functions $\mu = F(\mu, \gamma_{xa}, L_a/L_c, p, t)$ and $\alpha_{nx} = \alpha_{nx}(\mu, \gamma_{xa}, L_a/L_c, p, t)$ of the polycrystalline sample based on EMA [18, 20] are presented in detail. Notice that once having μ and α_{nx} it is easy to find α_{nz} since $\alpha_{nz} = \mu\alpha_{nx}$.

Now it is described how the experimental data is processed by means of the model.

From the Eq. (4), the tensor resistivity component of the paracoherent resistivity along the x-axis is given by the equation

$$\rho_{px} = \frac{1}{\alpha_{nx}(\mu, \gamma_{xa}, L_a/L_c, p, 1)}(\rho_{wl_x}). \tag{6}$$

Here, $t = 1$, because the grains are in the superconducting state. On the other hand, the extrapolation of the normal-state resistivity to zero temperature is given by a similar expression, but in this case $t \neq 1$ if the grains are anisotropic:

$$\rho_x(0) = \frac{1}{\alpha_{nx}(\mu, \gamma_{xa}, L_a/L_c, p, t)}(\rho_{wl_x}). \tag{7}$$

The ratio of Eqs. (6) and (7) gives

$$f_x = \frac{\rho_{px}}{\rho_x(0)} = \frac{\alpha_{nx}(\mu, \gamma_{xa}, L_a/L_c, p, t)}{\alpha_{nx}(\mu, \gamma_{xa}, L_a/L_c, p, 1)}, \tag{8}$$

which was experimentally determined. If we add to the Eq. (8) the equation of the anisotropy parameter μ, which was also experimentally determined

$$\mu = \frac{\alpha_{nx}(\mu, \gamma_{xa}, L_a/L_c, p, t)}{\alpha_{nz}(\mu, \gamma_{xa}, L_a/L_c, p, t)}, \tag{9}$$

a system of equations with γ_{xa} and t as unknown quantities is obtained. After finding γ_{xa} and t it is easy to obtain $A_{ab} = A_x\alpha_{nx}$ where α_{nx} is calculated and A_x is experimentally determined (see last blocks of Fig. 2).

As an example of how the model works the dependence of α_{nx} and α_{nz} as functions of γ_{xa} are shown in Fig. 7. The variation provoked by a 15 or 28 % of pores is quite small when $0.4 < \gamma_{xa} < 0.48$. The significant differences appear in the region of very low and very high values of γ_{xa}. The values of the intrinsic anisotropy parameter and shape anisotropy of the pollycrystalline sample were taken similar to those that will be used in this work.

3.4 Experimental verification of the model.

Let us analyse how the interpretation of the model outputs is supported by the experimental results (see Table 4). First, we have calculated the A_{ab} values by using two different expressions A_x/α_{nx} and A_z/α_{nz}. However, the difference between the obtained values does not exceed 2%. This result is supported by the behavior of μ as a function of the temperature displayed in Fig. 8. It exhibits a very small variation, 2% approximately, when T decreases from 300 K to the superconducting transition temperature for both samples. Such a behavior of μ is also reflected

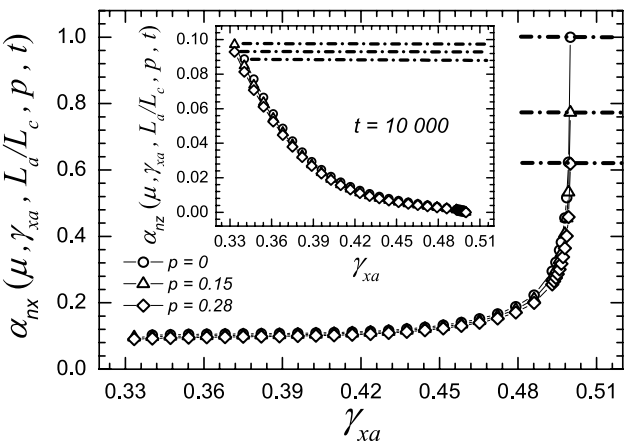

Fig. 7 α_{nx} as a function of γ_{xa} with $t = 10000$, $L_a/L_c = 20$ and three different values of p. Inset the same dependence for the case of α_{nz}. *The short dash dot lines* show the biggest difference between the dependencies with different values of p.

Table 4 Outputs parameters of the model displayed at the bottom of Fig. 2.

Sample	γ_{xa}	t	α_{nx}	α_{nz}	$A_{ab}=A_x/\alpha_{nx}$ (μΩ cm/K)	$A_{ab}=A_z/\alpha_{nz}$ (μΩ cm/K)	ρ_{wlx} (mΩ cm)	ρ_{wlz} (mΩ cm)
GD0P1	0.4299	16 849	0.1718	0.0092	0.983	0.993	0.117	0.114
GD0P2	0.4847	1 430	0.2950	0.0074	1.044	1.062	0.114	0.108

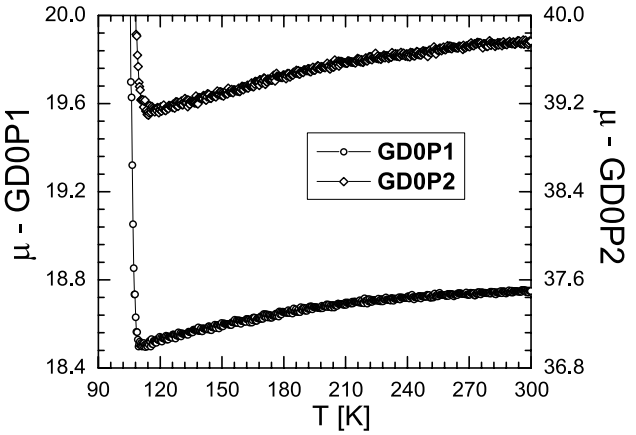

Fig. 8 Effective anisotropy parameter as a function of the temperature, $\mu(T)$, obtained from the ratio of the dependencies $\rho_i(T)$ (with $i = x, z$) measurements in GD0P1 and GD0P2 samples.

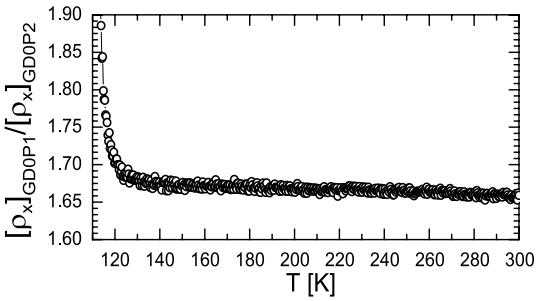

Fig. 9 Experimental verification of the ratio $[\rho_x]_{GD0P1}/[\rho_x]_{GD0P2} \simeq constant$ at different temperatures.

in the ρ_{wl} values which are very similar in the two main directions of the samples. Thus, one obtains $\mu = \alpha_{nx}/\alpha_{nz}$.

However, the obtained A_{ab} values are twice smaller than those reported elsewhere for single crystals without Pb doping [25] and by Fujii in his private communication. It seems to be that the doping with Pb has a great influence in the properties of the crystallites.

Another important issue, to be considered, is that the calculated γ_{ab} value is greater for the sample compacted at higher pressure GD0P2. This sample shows a greater orientation of its grains with the c axes parallel to the z axis as compared to the GD0P1 sample (see Fig. 3) . A third relevant issue can be found when A_{ab} and ρ_{wl} of both samples are compared. They are very similar. The differences do not surpass the 5%. Thus, one obtains $(\rho_{ab} + \rho_{wl})_{GD0P1} \simeq (\rho_{ab} + \rho_{wl})_{GD0P2}$, which implies $[\rho_x]_{GD0P1}/[\rho_x]_{GD0P2} \simeq$ constant, as it is experimentally verified when the samples are in the normal state (see Fig. 9.)

Finally, the experimental results shown in Fig. 6 may explain the great change of t with the compacting pressure. It suggests that the compacting pressure may change significantly the intragranular transport properties of the crystallites, contrary to the assumptions presented elsewhere [21, 22]. During the compacting process the grains may be mechanically deformed, provoking the increase of intragranular defects after the last thermal treatment as it was demonstrated in the subsection 3.1. It would decrease the effective anisotropy of the grains t. Moreover, it could be also the cause of the double step in the $\rho - J$ curves due to the modification of the critical current density in a part of the crystallites. It is symptomatic that there is a change of the slope in the $\rho_x - J$ curve that belongs to the GD0P2 sample at the same temperature where the grains of the GD0P1 sample starts the transition to the normal state.

On the other hand, according to our results, the decrease of t is linked to a drop in ρ_c component, since the A_{ab} values for both samples are practically the same. Such a drop may be supported by a decrease of the c parameter of the unit cell observed by Kocabaş et. al. [28] at high pelletization pressures.

Thus, both effects of a high pelletization pressure point toward a decrease of the effective anisotropy of the grains such as is obtained by the model application.

Another way to verify the model is to compare the experimental results of f_z direction with those predicted by the model. However, the $\rho_z(T)$ dependencies do not go completely to zero for temperatures at which the x component of resistivity is already zero as shown in Fig. 10. Such a effect provokes that the anisotropy factor μ of both samples increases during the superconducting transition of the samples instead of decreasing, as expected. Here, we identify a possible cause of this behaviour. It is related to the thin layer of Bi-2212 observed in the X-ray diffraction patterns of the pellets samples as discussed in subsection 3.1 . This film is in parallel for the measurements in the x-direction, but in series for the z direction, preventing the achievement of the zero resistivity in the $\rho_z(T)$ curve. Moreover, the oxygen loss and the micro strains are linked

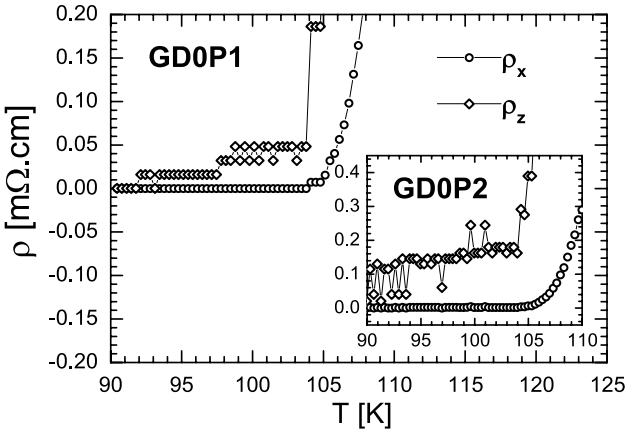

Fig. 10 $\rho_i(T)$ (with $i = x, z$) dependencies in the two main directions for both samples studied in this article.

to the presence of stacking faults [39] that may decrease the superconducting transition temperature in the c direction of the crystallites. It agrees with our experimental results, since the probability of finding ab planes in the z direction is lower in the case of the sample GD0P2, which exhibits a higher residual resistivity after the superconducting transition. In samples with high values of γ_{xa}, as the ones studied in this paper, the limit of percolation along the ab planes may be reached, thus producing the observed effect. Moreover, samples uniaxilly pressed exhibit a non-uniform distribution of the pressure effects in the compacting direction [40]. Thus, $\gamma_{xa}(x) \sim$ constant, but $\gamma_{za}(z)$ may decrease from the sample core to the surface. Here, $\gamma_{za}(z)$ represents the probability of finding grains with their a axis along the z direction of the sample. Such a behavior of the orientation probability is not included in the model, which assumes the superconducting ceramic as an anisotropic material, but an homogeneous one. Nevertheless, these effects can be disregarded for measurements performed in the normal state and those corresponding to the x direction.

4 Conclusions

By using an Effective Medium Approximation model applied to electric transport measurements of (Bi,Pb)2223 polycrystals, we have been able to determine the effective anisotropy of the grains, t, their orientation probability, γ_{xa}, the weak links resistivity, ρ_{wl}, and the slope of the temperature dependence of the grains' resistivity, A_{ab}. As far as the authors know, this self-consistent way of determining these parameters for a polycrystalline superconductors is reported by the first time. In addition, the correctness of the model has been experimentally demonstrated. An extension of our method to films and composite tapes would require, however, some modifications.

Our results for superconducting polycrystals show that high compacting pressures affect not only the intergranular, but also the intragranular transport properties by increasing the density of defects and reducing the effective anisotropy of the grains. The value of the effective anisotropy parameter of the grains, t, is similar to those reported in single crystals [25] without Pb doping, in the case of the GD0P1 sample. However, t decreases one order of magnitude when the compacting pressure is increased to the value used for the sample GD0P2 (780 MPa). In addition, the resistivity of the weak links, ρ_{wl}, does not change when the uniaxial compacting pressure increases although reduces the influence of microstructural defects such as voids and pores on the transport properties.

The effects of the pressure on the grains have not been detected before [21, 22] because these are masked by the influence of the compacting pressure on inter-granular properties, as shown by SEM micrographs.

The model, in its present form, does not work for the z direction of the samples, which is parallel to the compacting pressure direction. The observed dissipation along the z direction may be due to the thin layer of Bi-2212 detected in the x-ray diffraction patterns of the two pellet samples.

Acknowledgements This work was partially supported by CAPES/MES-CUBA, Projeto 104/10. We thank the support of PhD. R. Packard (University of California at Berkeley) and all the help by PhD. F. Calderón-Piñar and PhD. O. García-Zaldivar (Group of Ferroelectricity and Magnetism, IMRE-Physics Faculty, Havana University). We thank Professor PhD. Arbelio Pentón Madrigal (LAE, IMRE-Physics Faculty, Havana University) for useful discussions of X-ray difraction patterns.

Anisotropy parameter of polycrystalline samples with low-density of isotropic insulating defects

Let us see now, the method of calculating the anisotropy parameter of polycrystalline samples, with low-concentration of isotropic insulating defects [41] (with porosity included), present in volume fraction p. The application of EMA in this case is similar to that presented in reference [20], but considering the volume fraction of pores. For the x-axis we have:

$$(1-p)\left[\frac{2\gamma_{xa}(\sigma_a-\sigma_x)}{1+\frac{n_x}{\sigma_x}(\sigma_a-\sigma_x)}+\frac{\gamma_{xc}(\sigma_c-\sigma_x)}{1+\frac{n_z}{\sigma_x}(\sigma_c-\sigma_x)}\right]+ \\ +p\left[\frac{2/3(\sigma_p-\sigma_x)}{1+\frac{N_x}{\sigma_x}(\sigma_p-\sigma_x)}+\frac{1/3(\sigma_p-\sigma_x)}{1+\frac{N_z}{\sigma_x}(\sigma_p-\sigma_x)}\right]=0 \tag{10}$$

Here, $\sigma_a = 1/(\rho_a + \rho_{wl})$, $\sigma_c = 1/\rho_c$, $\sigma_x = 1/\rho_x$, $\sigma_z = 1/\rho_z$ and $\sigma_p = 0$. In addition, n_x, n_z, N_x and N_z are elements of the depolarization tensor of the grains, $\hat{n}$, and pores, $\hat{N}$, in the two main directions of the sample, respectively. The grains and pores are modelled as ellipsoids and spheres, respectively. The way of calculating the elements of $\hat{n}$ is [20]

$$n_x = n_y = \frac{1}{2}(1 - n_z);\ n_z = \frac{e^2+1}{e^3}[e - \arctan e] \tag{11}$$

where, $e = \sqrt{\mu(L_a/L_c)^2 - 1}$, is the eccentricity of the oblate ellipsoid [20]. The elements of $\hat{N}$ can be obtained by mean of the following expression [41]:

$$\begin{aligned} N_x = N_y &= \frac{\mu}{2(\mu-1)}\left[1 - \frac{\sinh^{-1}\sqrt{\mu-1}}{\sqrt{\mu(\mu-1)}}\right] \\ N_z &= \frac{1}{(\mu-1)}\left[1 - \sqrt{\mu}\frac{\sinh^{-1}\sqrt{\mu-1}}{\sqrt{\mu-1}}\right] \end{aligned} \tag{12}$$

Thus, the calculated average by means of Eq. (10) is similar to that obtained in the case of isotropic material with two different phases [18, 41]. These two phases correspond to the host material present in volume fraction $(1 - p)$ and the insulating defects that occupy the volume fraction p, respectively. At the same time the host material has two more different phases that correspond to the two main possible orientations of the grains along the x-direction of the sample, remembering that the conductivity along a and b axes in the host material are equivalent and their probabilities of orientation along the x-axis are the same, but they are different as compared with the c-axis. The values of 2 / 3 and 1 / 3 in Eq. (10) emerge from the assumption that the main axes of all insulating defects are randomly oriented. The possible intermediate orientations in the host material are disregarded in our approach as it was already mentioned. Starting from Eq. (10) and considering all the conditions described before, a quadratic equation, which is solved for σ_x can be obtained. The solutions for σ_x have the form,

$$\sigma_{x1,2} = \frac{-b_x \pm \sqrt{b_x^2 - 4a_x c_x}}{2a_x}\sigma_a = \alpha_{nx}\sigma_a \tag{13}$$

where

$$\begin{aligned} a_x = {} & (1-p)(N_x-1)(N_z-1)[2\gamma_{xa}(n_z-1)+ \\ & + \gamma_{xc}(n_x-1)] + \frac{p}{3}[2(N_z-1)+(N_x-1)]\times \\ & \times(1 - n_x - n_z + n_x n_z) \end{aligned}$$

$$\begin{aligned} b_x = {} & (1-p)(N_x-1)(N_z-1)\{2\gamma_{xa}(1-n_z)- \\ & - \gamma_{xc}n_x - \frac{1}{t}(2\gamma_{xa}n_z + \gamma_{xc}(n_x-1)]\}+ \\ & + \frac{p}{3}[2(N_z-1)+(N_x-1)][n_x(1-n_z) + n_z\frac{1}{t}(1-n_x)] \end{aligned}$$

$$\begin{aligned} c_x = {} & \frac{1}{t}\{(1-p)(N_x-1)(N_z-1)[2\gamma_{xa}n_z + \gamma_{xc}n_x]+ \\ & + \frac{p}{3}[2(N_z-1)+(N_x-1)]n_x n_z\} \end{aligned}$$

Here, the condition of probability sum is $2\gamma_{xa} + \gamma_{xc} = 1$. Similarly, for the z axis one obtains

$$\begin{aligned} & (1-p)\left[\frac{2\gamma_{xc}(\sigma_a - \sigma_z)}{1 + \frac{n_x}{\sigma_z}(\sigma_a - \sigma_z)} + \frac{\gamma_{xa}(\sigma_c - \sigma_z)}{1 + \frac{n_z}{\sigma_z}(\sigma_c - \sigma_z)}\right]+ \\ & + p\left[\frac{1/3(\sigma_p - \sigma_z)}{1 + \frac{N_x}{\sigma_z}(\sigma_p - \sigma_z)} + \frac{2/3(\sigma_p - \sigma_z)}{1 + \frac{N_z}{\sigma_z}(\sigma_p - \sigma_z)}\right] = 0 \end{aligned} \tag{14}$$

This equation is solved for σ_z with solutions similar to Eq. (13) and parameters:

$$\begin{aligned} a_z = {} & (1-p)(N_x-1)(N_z-1)[2\gamma_{xc}(n_z-1)+ \\ & + \gamma_{xa}(n_x-1)] + \frac{p}{3}[2(N_x-1)+(N_z-1)]\times \\ & \times(1 - n_x - n_z + n_x n_z) \end{aligned}$$

$$\begin{aligned} b_z = {} & (1-p)(N_x-1)(N_z-1)\{2\gamma_{xc}(1-n_z)- \\ & - \gamma_{xa}n_x - \frac{1}{t}(2\gamma_{xc}n_z + \gamma_{xa}(n_x-1)]\}+ \\ & + \frac{p}{3}[2(N_x-1)+(N_z-1)][n_x(1-n_z) + n_z\frac{1}{t}(1-n_x)] \end{aligned}$$

$$\begin{aligned} c_z = {} & \frac{1}{t}\{(1-p)(N_x-1)(N_z-1)[2\gamma_{xc}n_z + \gamma_{xa}n_x]+ \\ & + \frac{p}{3}[2(N_x-1)+(N_z-1)]n_x n_z\} \end{aligned}$$

Finally, starting from the description of the model discussed in item 3.3 the expression for the anisotropy parameter becomes a transcendental equation with the form,

$$\begin{aligned} \mu = {} & \frac{\sigma_x}{\sigma_z} = \frac{\alpha_{nx}(\mu, \gamma_{xa}, \frac{L_a}{L_c}, p, t)}{\alpha_{nz}(\mu, \gamma_{xa}, \frac{L_a}{L_c}, p, t)} = \\ = {} & F(\mu, \gamma_{xa}, L_a/L_c, p, t) \end{aligned} \tag{15}$$

which can be solved through the method of successive iterations as described elsewhere [42].

Analytical procedure for Levin-Gonzalez' method

We have applied the measurement model proposed by González et al. [23] for measuring the different components of the resistivity tensor in $Bi_{1.65}Pb_{0.35}Sr_2Ca_2Cu_3O_{10+\delta}$ polycrystalline superconductors. For the ρ_z experimental determination, the current is injected onto the top surface of the sample and extracted at the bottom. Two aligned contacts recording the voltage are located according to Fig. 1c. In the quasistatic limit, the expression which satisfies the Laplace's differential equation with the first boundary condition is [23]:

$$V(x,z) = V_0 z + \sum_{n=1}^{\infty} V_n \cos\left(\frac{n\pi x}{L}\right) \times \times \sinh\left[\frac{n\pi\sqrt{\rho_z}}{\sqrt{\rho_x}L}(D/2 - z)\right] \tag{16}$$

Hence, the V_0 and V_n coefficients can be found through the Fourier methods using the last boundary condition on the transport current applied. Here, we just give the explicit coefficients, leaving the detailed development for Appendix A in reference [23]: $V_0 = I\rho_z/bL$ and $V_n = -2I/n\pi b\cosh(n\pi\sqrt{\rho_z}D/2\sqrt{\rho_x}L)$. Establishing that the voltage signal in a measurement is $\Delta V = V(x_0, D) - V(x_0, 0)$ and taking in account Eq. (16) where it has been substituted the V_0 and V_n dependence, it can be deduced an expression for the measured resistance as a function of the parameters of the sample $\sqrt{\rho_x}$, $\sqrt{\rho_z}$, D, b and L:

$$R_z = \frac{\rho_z D}{bL}\left[1 + \sum_{n=1}^{\infty} \frac{4L\cos(\frac{n\pi x_0}{L})\tanh(\frac{n\pi\sqrt{\mu}D}{2L})}{n\pi\sqrt{\mu}D}\right] \tag{17}$$

where $\mu_{=}\rho_z/\rho_x$. An important point here is that the series for R_z is a slowly (conditionally) converging one, which *cannot be truncated* for any value of anisotropy $\sqrt{\mu}$, large or small. This is a common feature of the potential distributions due to arrays of charges [43]. A way to solve this problem is to separate the slowly converging series of R_z into slowly and rapidly converging parts in such a way that would allow to carry out the summation of the slowly converging part exactly (analytically or numerically). For example, Eq. (17) can be rewritten as follows:

$$R_z = \frac{4\sqrt{\rho_z\rho_x}}{b\pi}\left[\frac{\pi\sqrt{\mu}D}{4L} + Y_z(x_0) + S_z(\sqrt{\mu})\right] \tag{18}$$

where

$$Y_z(x_0) = \sum_{n=1}^{\infty}\frac{\cos(n\pi x_0/L)}{n} = \ln\left[2\sin\left(\frac{\pi x_0}{2L}\right)\right] \tag{19}$$

and

$$S_z(\sqrt{\mu}) = \sum_{n=1}^{\infty}\frac{\cos(\frac{n\pi x_0}{L})}{n}\left[\tanh\left(\frac{n\pi\sqrt{\mu}D}{2L}\right) - 1\right] \tag{20}$$

The term $Y_z(x_0)$ is reported in reference [23] and characterizes the sample's geometry, but does not depend on the resistivity. On the other hand, $S_z(\sqrt{\mu})$ is a rapidly (exponentially) converging series, which can be truncated and therefore lends itself easily to numerical evaluation even for relatively small values of anisotropy such that $\frac{\pi\sqrt{\mu}D}{2L} \sim 1$.

The other configuration in which the contacts are located on the face perpendicular to the z-axis, as in Fig. 1b, was analyzed by reference [24] in the single harmonic approximation and for a multi-terminal contact configuration. By using analogous boundary conditions on the current like in the paragraphs above, it is easy to show that the final expression for the resistance in this configuration is [24]:

$$R_x = \frac{8\sqrt{\rho_z\rho_x}}{b\pi}\left[Y_x(l) + S_x(\sqrt{\mu})\right] \tag{21}$$

where

$$Y_x(l) = \sum_{n=1}^{\infty}(-1)^{n-1}\frac{\cos[\pi l(2n-1)/2L]}{2n-1} = = \frac{1}{2}\ln\left[\tan\left(\frac{\pi}{4} + \frac{\pi l}{4L}\right)\right] \tag{22}$$

and

$$S_x(\sqrt{\mu}) = \sum_{n=1}^{\infty}(-1)^{n-1}\frac{\sin\left[\frac{(2n-1)\pi l}{2L}\right]}{2n-1} \times \times \left[\coth\left[\frac{(2n-1)\pi\sqrt{\mu}D}{L}\right] - 1\right] \tag{23}$$

In references [24, 44] was reported than even for the samples with the lowest anisotropy ($\frac{\pi\sqrt{\mu}D}{2L} \sim 1$) it was sufficient to retain only the first three terms, $n = 1, 2, 3$, to obtain convergence of the results better than 0.1% [24, 44]. For that reason in the series given to Eqs. (18) and (21) only the first three terms will be taken into consideration. From the ratio R_z/R_x, they can be obtained all values of anisotropy $\sqrt{\mu}$ after solving a transcendental equation. The result may be substituted into Eqs. (18) and (21) and both resolved later to give the true resistivities ρ_x and ρ_z, through the following expressions:

$$\rho_x = \frac{R_x b\pi/8\sqrt{\mu}}{\left\{\frac{1}{2}\ln\left[\tan\left(\frac{\pi}{4}+\frac{\pi l}{4L}\right)\right]+S_x(\sqrt{\mu})\right\}^{-1}} \quad (24)$$

and

$$\rho_z = \frac{R_z\sqrt{\mu}b\pi/4}{\left\{\frac{\sqrt{\mu}\pi D}{4L}+\ln[2\sin(\frac{\pi x_0}{2L})]+S_z(\sqrt{\mu})\right\}^{-1}} \quad (25)$$

References

1. S. Safran, A. Kılıç, O. Ozturk, J. Mater. Sci. **28**(2), 1799–1803 (2016)
2. C. Kaya, B. Özçlik, B. Özkurt, A. Sotelo, M. A. Madre, J. Mater. Sci. **24**, 1580–1586 (2013)
3. C.L. Carvalho, K. Yukimitu, V.C.S. Reynoso, J.C.S. Moraes, E.B. Aaraújo, N. Aalves, S. Rainho, J. Mater. Sci. **16**, 135–138 (2005)
4. W.M. Woch, M. Chrobak, M. Kowalik, R. Zalecki, M. Giebułtowski, J. Niewolski, Ł. Gondek, J. Alloys Compd. **692**, 359–363 (2017)
5. J.-C. Grivel, X.P. Yang, A.B. Abrahamsen, Z. Han, N.H. Andersen, von M. Zimmermann, J. Phys. **234**, 022012 (2010)
6. H. Hosono, K. Tanabe, E. Takayama-Muromachi, H. Kageyama, S. Yamanaka, H. Kumakura, M. Nohara, H. Hiramatsu, S. Fujitsu, Sci. Technol. Adv. Mater. **16**, 033503 (2015)
7. P. Mele, R. Guzman, J. Gazquez, T. Puig, X. Obradors, S. Saini, Y. Yoshida, M. Mukaida, A. Ichinose, K. Matsumoto, M. I. Adam, Supercond. Sci. Technol. **28**, 024002 (2015)
8. G. Naderi, J. Schwartz, Supercond. Sci. Technol. **27**, 115002 (2014)
9. H. Koralay, O. Hicyilmaz, S. Cavdar, E. Asikuzun, A. T. Tasci, O. Ozturk, J. Mater. Sci. **25**, 3116–3126 (2014)
10. M. Pakdil, E. Bekiroglu, M.Oz, N.K. Saritekin, G. Yildirim, J. Alloys Compd. **673**, 205–214 (2016)
11. Ş. Yavuz, Ö. Bilgili, K. Kocabaş, J. Mater. Sci. **27**, 4526–4533 (2016)
12. V. Grinenko, G. Fuchs, K. Nenkov, C. Stiehler, M. Vojenčiak, T. Reis, B. Oswald and B. Holzapfel, Supercond. Sci. Technol. **25**, 075006 (2012)
13. M. Sahoo and D. Behera, J Mater. Sci. Eng. **1**(4), 2–7 (2012)
14. D. Marconi, C. Lung, A.V. Pop, J. Alloy Compd. **579**, 355–359 (2013)
15. E. Altshuler, S. García, J. Barroso, Phys. C **177**, 61 (1991)
16. C.P. Bean, Rev. Mod Phys. **36**, 31 (1994)
17. A. Yıldız, K. Kocabaş, G.B. Akyüz, J. Supercond. Nov. Magn. **25**, 1459–1467 (2012)
18. D. Stroud, Phys. Rev. B **12**, 3368 (1975)
19. A. Díaz, J. Maza, F. Vidal, Phys. Rev. B **55**, 1209 (1997)
20. A. Cruz-García, P. Muné, Phys. C **527**, 74–79 (2016)
21. E. Govea-Alcaide, P. Muné, R.F. Jardim, Braz. J. Phys. **35**(3A), 680 (2005)
22. E. Govea-Alcaide, R.F Jardim, P. Muné, Phys. Stat. Sol. **13**, 2484 (2005)
23. J. L. González, J.S. Espinoza Ortiz, E. Baggio-Saitovitch, Phys. C **315**, 271 (1999)
24. G.A. Levin, J. Appl. Phys. **81**, 714 (1997)
25. T. Fujii, T. Watanabe, A. Matsuda, Phys. C **357**, 173 (2001)
26. P. Muné, E. Govea-Alcaide, and R. F. Jardim, Phys. C **384**, 491 (2003)
27. X. Yang, T.K. Chaki, Supercond. Sci. Technol. **6**, 343–348 (1993)
28. K. Kocabaş, M. Gökçe, M. Çiftçioğlu, Ö. Bilgili, J. Supercond. Nov. Magn. **23**, 397–410 (2010)
29. M. Hernández-Wolpez, A. Cruz-García, O. Vázquez-Robaina, R. F. Jardim, P. Muné, Phys. C **525–526**, 84 (2016)
30. T.T. Tan, S. Li, H. Cooper, W. Gao, H.K. Liu, S.X. Dou, Supercond. Sci. Technol. **14**, 471 (2001)
31. C.W. Chiu, R.L. Meng, L. Gao, Z.J. Huang, F. Chen, Y.Y. Xue, Nature **365**, 323 (1993)
32. S.A. Halim, S.A. Khawaldeh, S.B. Mohammed, H. Azhan, Mater. Chem. Phys. **61**, 251 (1999)
33. D. Pandey, R. Mahesh, A.K. Singh, V.S. Tiwari, Phys. C **184**, 135 (1991)
34. B.D. Cullity, *Elements of X-ray Diffraction*, 2nd edn. (Addison-Wesley, Reading, 2001), pp. 284–292
35. J. M. Yoo, K. Mukherjee, Phys. C **222**, 241–251 (1994)
36. F. K. Lotgering, J. Inorg. Nucl. Chem. **9**, 113 (1959)
37. V.N. Zverev, D.V. Shovkun, I.G. Naumenko JETP Lett. **68**, 332 (1998)
38. V.N. Zverev, D.V. Shovkun, JETP Lett. **72**, 73 (2000)
39. V. Kataev, N. Knauf, B. Büchner, D.Wohlleben, Phys. C **184**, 165 (1991)
40. E. Govea-Alcaide, M. Hernández-Wolpez, A.J. Batista-Leyva, R.F. Jardim, P. Muné, Phys. C **423**, 51–56 (2005)
41. J. Garner, D. Stroud, Phys. Rev. B **25**, 3199 (1982)
42. N.I. Danílina, N.S. Dubrósvskaya, O.P. Kvashá, G.L. Smirnov, Matemática de Cálculo, (Editorial Mir Moscú, 1990), pp. 190
43. B.F. Logan, S.O. Rice, R.F. Wick, J. Appl. Phys. **42**, 2975 (1971)
44. J. Jiang, D. Stroud, Phys. Rev. B **25**, 3199 (1982)